Advanced Dual-Core Photonic Crystal Fiber Plasmonic Biosensor: Unveiling High Sensitivity and Practical Feasibility for Biochemical Detection

Sapana Yadav[1] · D. K. Dwivedi[1] · Pooja Lohia[2] · Yadvendra Singh[3]

Abstract

The article proposes a dual-core photonic crystal fiber-based plasmonic biosensor. Two prominent hexagonal lattices with circular air holes along with plasmonic material and analyte sensing layer have been deposited on the outer surface of the fiber to make the practical applications feasible. A thickness of 30 nm of noble plasmonic material silver has been applied to excite the surface plasmons. A 5-nm-thin titanium dioxide (TiO_2) layer has also been observed as an adhesive layer between the silica glass and silver. The behavior of the sensor has been examined employing the mode solver-based finite element method (FEM). The proposed sensor gives responses of maximum amplitude sensitivity of 98.67764 RIU^{-1} and maximum wavelength sensitivity of 14,090 nm/RIU in the *y*-polarized propagation mode, employing the amplitude and wavelength interrogation methods, respectively. Furthermore, with the variation of concentration of β-LG, it shows maximum amplitude sensitivity of 110.59998 RIU^{-1} and WS of 5303.253 nm/RIU. Owing to the straightforward design and maximum sensitivity, the proposed sensor can be applicable to detect biological and biochemical samples.

Introduction

In recent decades, photonic crystal fiber (PCF) has supplanted traditional fiber optics, and with technological progress, it has increasingly integrated with surface plasmon resonance (SPR) to offer exceptional sensing capabilities and user-friendly functionality [1]. PCF-based SPR sensors have some advantages as compared to the traditional prism-based sensors. In prism-based sensors, SPR takes place at specific incident angles of incoming light, necessitating various mechanical components, whether fixed or movable, to achieve these conditions [2, 3]. This mechanical complexity adds bulkiness to the complete experimental setup. To overcome these limitations, in 1993, Jorgenson introduced PCF-SPR-based bioinstrumentation [4]. On the contrary, PCF offers several advantages, including cost-effectiveness, compactness, and robustness making it a desired choice for sensing detection and higher sensitivity as compared to the fiber and prism based SPR sensors. Furthermore, PCF sensors offer the significant advantage of easy resonance wavelength (RW) tuning by adjusting various parameters (such as air hole size and pitch distance) during fabrication [5]. Selecting the right plasmonic material is also crucial to achieve strong excitation of plasmon waves on the PCF surface. In the literature, gold is often favored as the greatest striking plasmonic material in PCF-based sensors due to its high chemical stability and biocompatibility [6]. Gold exhibits a larger resonance wavelength shift than other plasmonic materials. However, it is worth noting that this choice can lead to broader resonance peaks which gives low sensing range. Silver can be used as a noble plasmonic material to address this issue, offering narrower resonance peaks and attaining higher sensitivity with better detection accuracy (DA) [7]. Nonetheless, silver is susceptible to rapid oxidation in humid environments, potentially compromising the accuracy of

✉ D. K. Dwivedi
todkdwivedi@gmail.com

1   Photonics and Photovoltaic Research Lab (PPRL), Department of Physics and Material Science, Madan Mohan Malaviya University of Technology, Gorakhpur, India 273010

2   Department of Electronics and Communication Engineering, Madan Mohan Malaviya University of Technology, Gorakhpur, India 273010

3   School of Electrical Engineering and Computer Science, Oregon State University, Corvallis, OR 97331, USA

analyte detection. To overcome the rapid oxidation of the silver and to enhance surface to volume ratio, a few nanometers thick TiO_2 coating has been incorporated on the top of the silver layer. By harnessing the unique properties of PCF, SPR-based sensors employ a range of sensing mechanisms. These include slotted-based, nanowire-based, and both external and internal metal coating-based approaches [8, 9]. Among these techniques, internal and external metal coating-based sensing methods are the most generally employed [9–11].

Lately, this approach has gained extensive popularity for photonic crystal fiber-surface plasmon resonance sensing applications due to its simple and highly practical identification capabilities [12]. When assessing sensitivity, it is crucial to contemplate a design that enables a streamlined manufacturing process while attaining outstanding high-performance features [13]. In a study by Wang et al. a PCF-SPR design based on a D-shaped biosensor demonstrated a wavelength sensitivity (WS) of 3340 nm/refractive index unit (RIU) [14]. However, achieving such high sensitivity often requires excessive surface polishing, which can pose manufacturing challenges. In another study focused on external detection, Hasan et al. reported a sensor with a maximum amplitude sensitivity (AS) of 371.5 RIU^{-1} and a WS of 4600 nm-RIU^{-1}, although, in this study, the AS was not as high compared to some other designs. Recently, there has been research on surface plasmon resonance-based diamond ring optical fiber sensors. This study introduced a diamond ring PCF-SPR sensor, demonstrating a maximum WS of 6000 nm/RIU within a sensing range spanning from 1.33 to 1.39 RIU [14]. Additionally, another open ring channel-based PCF-SPR biosensor was studied in the same study, which showcased its capability to detect small variations in refractive indices (RI) of real-time analytes, ranging from 1.23 to 1.29 RIU. This sensor exhibited an average WS of 5500 nm-RIU^{-1} and an AS of 333.8 RIU^{-1} [15]. The envisioned exhibition of the PCF holds significant promise for refractive index (RI) sensing applications, thanks to its noteworthy sensing capabilities. Biosensors play a crucial role in various fields such as healthcare, environmental monitoring, and food safety by providing real-time and sensitive detection of biological and biochemical substances. However, existing biosensor technologies often face limitations in terms of sensitivity, practicality, and ease of fabrication [16]. Addressing these limitations while introducing novel features is essential for advancing biosensor capabilities. The proposed dual-core photonic crystal fiber-based plasmonic biosensor addresses these limitations through several novel features and design choices like Plasmonic Enhancement, Compact and Practical Design, Simplified Fabrication, High Sensitivity, and Versatility. Further, several numerical methods have been developed for biosensing applications. Various advantages

like ease of operation and design, a lower identification threshold, provide electrochemical biosensor. To identify the change in mass due to biomolecular interaction proposes piezoelectric sensor using the piezoelectric effect. To check the thermodynamic changes that emerge as a result of the cascade effect of physiological effect can be utilized as temperature biosensors. Recently, optical biosensing has gained significant attention as a technique in the field of biosensing. The operation of optical biosensors relies on the principle that the detection of an analyte molecule initiates a series of events leading to either the emission or absorption of light. Surface plasmon resonance (SPR), luminescence, absorption, and fluorescence are various techniques for biosensing in optical biosensors.

Milk infections are currently an important threat to public health, particularly among babies [17]. Lactoglobulin (β-LG) is a compact, globular-form allergenic protein present in the milk of various mammals. Therefore, considering β-LG, a key allergen, for diagnosis is a preferred choice. The β-LG monomer has a standard size of diameter 3 nm, comprising 162 amino acid residues, and possesses a molar mass of 18.40 k Da. Numerous biosensors to identify milk proteins, particularly β-LG, have been proposed [18]. The present paper explores a theoretical analysis of a SPR sensor based on DC-PCF. The sensor design presents a hexagonal lattice structure with circular air holes, which contributes to its simplicity. Sensor's performance has been investigated employing the Finite Element Method (FEM) with a circular Perfectly Matched Layer (PML) boundary condition [19]. The sensor identifies lower concentration of the biomolecules with the property of PCF-SPR in considerably limiting the electric field in the narrower small RI core area. Accomplish all the investigation using β-LG molecules in a liquid state as a particular case; however, the outcomes may be applied to identify other tiny molecules as well. The core switched to β-LG molecules, creating an adlayer of the biomolecule. Hence, the RW shifts spectrally because of β-LG molecule concentration. The present system depends on the very precise spectral interrogation technique, which quantifies variations in the biosamples refractive index and thickness of affinity layer by monitoring spectral shifts in the RW. However, a more realistic approach has been devised and used to measure the refractive index of an adlayer produced via surface sensing. Through optimization of structural parameters, enhanced sensitivity in terms of amplitude sensitivity, wavelength sensitivity, and Figure of Merit (FOM) have been achieved. Present analysis is geared toward maximizing these key sensor characteristics. The highly sensitive nature of this sensor, combined with its straightforward structure, offers promising prospects for practical implementation in various optical sensing applications [20]. By employing the FEM numerical approach, the optical and dielectric characteristics of the offered biosensor as it guides electromagnetic

waves in the Vis–NIR spectrum within the fiber core have been analyzed. The "Introduction" section presents the state of art of the present work. A brief outline of the device's geometry and the fundamental physical principles governing its operation is presented in the "Design and Theoretical Backdrop" section. The "Formulation and Theoretical Interpretation" section provides a detailed explanation of the specific FEM techniques utilized in this study. Moving forward, the "Optimization of Sensor" section includes results and discussion, which is devoted to the analysis and discourse on the obtained outcomes. The "Performance analysis of the sensor" section shows experimental fabrication possibility. Finally, the concluding remark is presented in the "Fabrication Feasibility and Applicability" section.

Design and Theoretical Backdrop

Design Considerations

The sensor is designed using the Finite Element Method (FEM) in COMSOL Multiphysics 5.1 [21]. Upon launching the program, a two-dimensional model (2D) is selected for the space dimension. The chosen physics is Electromagnetic Wave, Frequency Domain (ewfd), and the study type is set to mode analysis. Subsequently, the geometries, materials, and mesh type are specified to measure the sensor's confinement loss based on the imaginary portion of the effective refractive index (n_{eff}) of the fundamental mode. The cross-sectional view of the proposed sensor with different layers is shown in Fig. 1a. The two hexagonal rings are organized by lattice air holes, maintaining consistent center-to-center distances referred to as the pitch (p). The phase-matching properties can be made easier by a smaller air hole with a diameter of (d_c) in the middle. To implement the dual-core scheme, two of the inner ring's air holes are eliminated. Regular air holes have a (d) diameter. Four scaled-down (d_2) and two scaled-up (d_1) air holes in the outlying ring help to create a robust coupling between the surface plasmon polaritons (SPPs) wave. These air holes result adequate space to propagate light effectively through the metal-dielectric surface and improve sensitivity [6].

For practical sensing, a schematic experimental setup is depicted in Fig. 1. An optical tunable source (OTS) is required to launch the incoming light, and a polarizer accompanying a polarizer controller is required to transmit the light. Through single-mode fiber (SMF), linearly polarized light has been launched into the proposed sensor. A splicing method can be initiated in the proposed sensor to couple the SMF. The inlet and outlet of the liquid analyte are aided using an analyte flow tube that lies at the external border. It is possible to preserve the analyte intake and outflow by employing a pump. The change in the effective

refractive index of the plasmonic mode owes shift in the signal's wavelength, which occurs with the interaction of the analyte and ligand. The optical spectrum analyzer (OSA) is employed to compute the transmitted light, linked with a sensor by other SMF. With the help of an output spectrum, the shifting of wavelength can be noticed and examined on the computer. Blue shift occurs when the RW shifts toward the lower wavelength; on the contrary, shift toward the large wavelength is known as red shift.

Selection of RI

Fused silica has been employed as the background material whose wavelength-dependent refractive index can be evaluated employing the following Sellmeier Eq. (1) [22].

$$n_s{}^2(\lambda) = 1 + \frac{B_1\lambda^2}{\lambda^2 - C_1} + \frac{B_2\lambda^2}{\lambda^2 - C_2} + \frac{B_3\lambda^2}{\lambda^2 - C_3} \tag{1}$$

where $n_s(\lambda)$ is refractive index at a specified wavelength (λ) in (μm) and λ represents the wavelength of light source. $B_{(i=1,2,3)}$ and $C_{(i=1,2,3)}$ denote material-particular coefficients that can be taken from reference [23]. The variation of RI of fused silica changes 1.28×10^{-5} (per degree Celsius) only in response to temperature. Consequently, in typical environments with no significant temperature fluctuations, the impact of temperature can be disregarded.

The sensor's plasmonic component consists of a small silver layer. The Drude model is suitable for determining the dielectric permittivity of silver metal. This model analytically approximates the dielectric function associated with intra-band transitions of conduction electrons as they interact with an electromagnetic wave. When experienced in an electric field, the dielectric function is further modified by the polarization of electrons in the innermost coatings of noble metals, indicating optical shift from the valence bands to conduction bands. The expression of the Drude model for a thin silver film is followed by Eq. (2) [7]:

$$\epsilon_{\text{Ag}} = \epsilon_\infty - \frac{\omega_D^2}{\omega(\omega + j\gamma_D)} - \frac{\Delta\epsilon\Omega_L^2}{(\omega^2 - \Omega_L^2) + j\Gamma_L\omega} \tag{2}$$

The symbol denotes ϵ_{Ag} the dielectric constant of silver, $\epsilon_\infty = 5.9673$ high frequency permitivity, ω_D plasma frequency, ω angular frequency and γ_D damping frequency, $\Delta\epsilon$ weight coefficient, Ω_L oscillator strength, and Γ_L Lorentz oscillator's frequency width. The merits have been used from the reference.

Between the Ag layer and the silica glass, a thin TiO_2 coating has been utilized. The Ag has weak adherence without the TiO_2 coating and easily flakes off with light pressure. The required adherence can be provided by a coating of TiO_2. Additionally, TiO_2 film has a maximum refractive
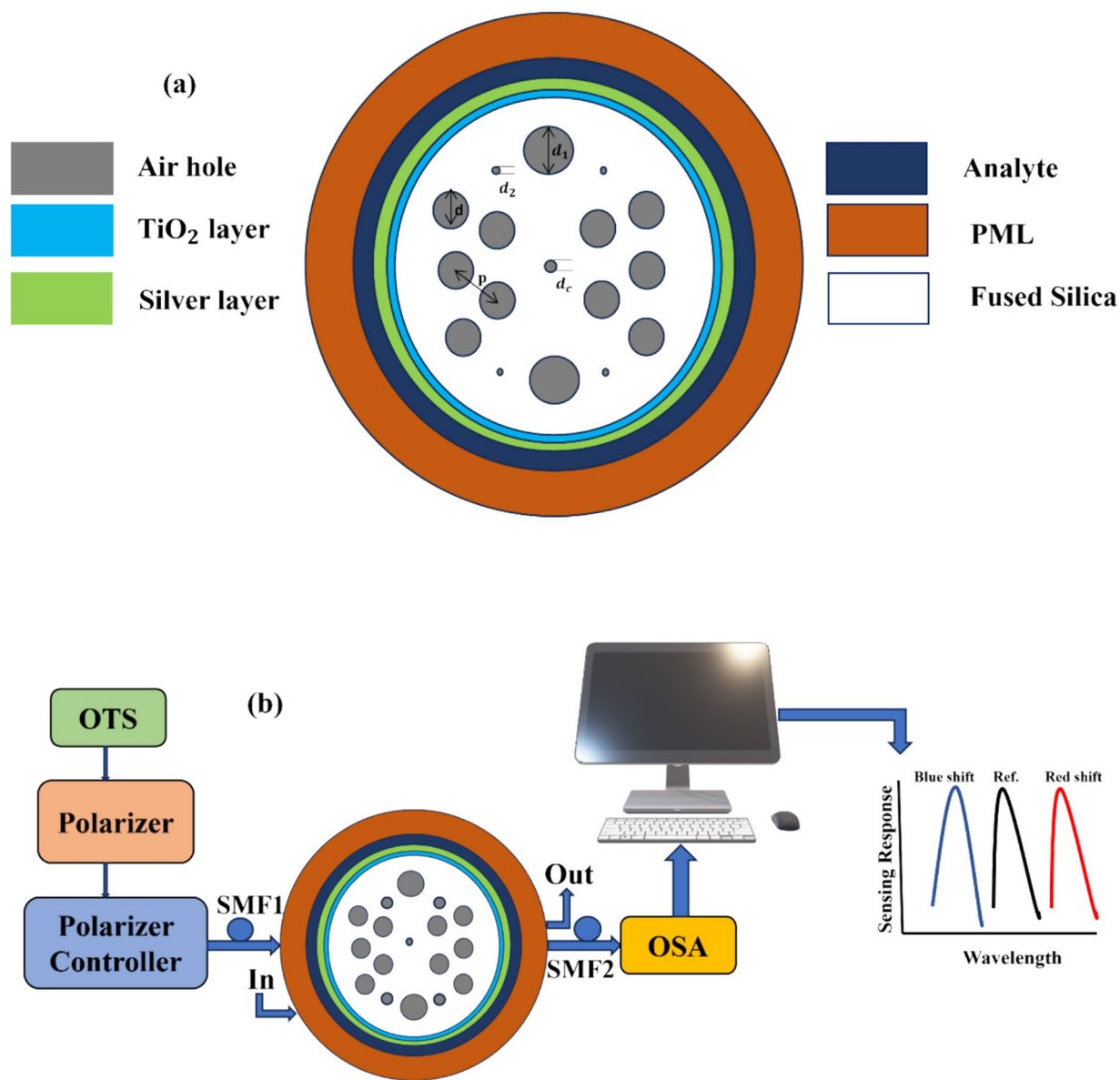
Fig. 1 **a** 2D illustrative cross-sectional view and **b** developmental layout of the offered sensor

index and functions as a transition metal that can produce a significant number of electrons at the surface. This generates a potent evanescent wave that pulls the core mode into the SPP mode and intensifies their interaction. The RI of TiO_2 film can be obtained employing the Eq. (3) [24].

$$n_{TiO_2}^2 = 5.913 + \frac{2.441 \times 10^7}{\lambda^2 - 0.803 \times 10^7} \tag{3}$$

where n_{TiO_2} denotes the RI of TiO_2 and λ represents the operating wavelength (μm). On the outer surface of the PCF, it is crucial for the biosensor to deposit consecutively Ag and TiO_2 layer. The refractive index (n_p) of β-LG can be

formulated employing a two term Cauchy Eq. (4) given below [20]:

$$n_p = B + \frac{9.6 \times 1010^3}{\lambda^2} \tag{4}$$

where the intercept B for β-LG has been taken 1.568.

For different concentration of β-LG in water, the dielectric constant of the bio-sample (ϵ_{se}) can be calculated employing Maxwell-Garnet effective medium theory with the help of Eq. (5) [20].

$$\sum_m \frac{\epsilon_m - \epsilon_{se}}{\epsilon_m + 2\epsilon_{se}} v_m = 0 \tag{5}$$

From this equation, v_m and ($\in_m = n_m^2$) denote volume fraction of the *m*th component and the dielectric constant, respectively.

The unit cell of β-LG protein layer (restricted in the core area) forms a consistent cubic layer that contains spherical β-LG molecules along with water molecules. The dielectric molecule of this effective layer ($\in_x$) can be determined employing superposition principle with the help of Eq. (6) [20].

$$\in_x = \frac{\in_p v_p + \varepsilon_{\text{water}} v_{\text{water}}}{v_t} \qquad (6)$$

From this equation, $\varepsilon_{\text{water}}$ and ($\in_p = n_p^2$) denote water molecule and dielectric constants of β-LG. While v_p, v_t, and v_{water} signify the volume employed by spherical β-LG molecule, total volume of the cubic unit cell, and volume employed by water molecules, respectively.

The molar concentration of β-LG per layer can be evaluated employing given Eq. (7) below [20]:

$$\text{Molarity} = \frac{\text{No. of moles of } \beta\text{-LG}}{\text{Volume of solution}} \qquad (7)$$

$$\text{No. of moles of } \beta\text{-LG} = \frac{\text{Mass of } \beta\text{-LG}}{\text{Molar mass of } \beta\text{-LG}} \qquad (8)$$

The molar mass and mass of a β-LG molecule is 18,400 gmol^{-1} and 1.88 g $\times 10^{-20}$, respectively. On supposing the β-LG molecules dilation in 1 ml of water, the molar concentration of β-LG monomer can be calculated as 0.75 fM. The molar concentration for a single layer including dimers will be doubled to 1.5 fM. The density of β-LG protein molecule has been used as 1.33 g/cc in the proposed work.

Alteration of molar concentration M in g/ml:

$$\text{Concentration} = \text{molar mass} \times \text{molar concentration (gml}^{-1}) \qquad (9)$$

1 M of β-LG = 1 mole l^{-1} *of* β-LG 1 mole l$^{-1} \times$ 18400 gmole^{-1}
$$= 18400 \text{ gl}^{-1} = 18.4 \text{ gml}^{-1}$$

With the help of this Eq. (9), molar concentration can be simply transformed into g ml^{-1} concentration easily by multiplying the molar mass of the molecule.

Formulation and Theoretical Interpretation

Numerical simulation methods are valuable tools for designing and predicting the optical behavior of biosensors. These methods permit for a quick initial assessment of sensor performance and allow insights into the included optical event, all while lowering optimization and development. In reference to transmitting waves through intricate structures, the finite element method (FEM)-based COMSOL Multiphysics 5.4 is the preferred choice.

A key advantage of FEM is its exceptional adaptability. It permits a precise representation of all geometry and the seamless inclusion of materials with intricate, time-dispersive, and anisotropic characteristics. In comparison to conventional resolution techniques, FEM enables the handling of complex material properties and introduces novel opportunities for analysis of nonlinear properties [25].

To enhance the performance of element quality and performance accuracy, extremely fine mesh element size with electromagnetic wave frequency domain (ewfd) has been used during simulation. The complete mesh consists of 151,616 domain elements and 17,592 boundary elements. The properties of mesh elements are defined here: to ensure better simulation accuracy, the complete mesh area consists of 397 μm^2 and average element quality 0.2919. The number of vertex, triangular, and edge elements are 84, 17,432, and 150,416, respectively. To investigate the characteristics of confinement loss for distinct analytes can be formulated using the given Eq. (10) [26]:

$$\alpha_1 = 8.686 \times \frac{2\pi}{\lambda} \times \text{Img}(n_{\text{eff}}) \times 10^4 \left(\frac{\text{dB}}{\text{cm}} \right) \qquad (10)$$

Here, λ expresses the operating wavelength (μm) and n_{eff} effective refractive index. It has been noticed that owing to the change in analyte's RI (1.36 to 1.41), having 0.001 step size shows significant impact on the loss spectrum. For $n_a = 1.36$, a smaller loss spectrum, whereas for $n_a = 1.41$, higher loss spectrum has been achieved. The higher power switches from core mode to SPP mode when the loss spectra are high. In general, the SPP mode shows high sensitivity when varying the RI of analytes. Sensitivity can be calculated for a particular wavelength with amplitude interrogation technique from the given Eq. (11) [4]:

$$S_A = -\frac{1}{\alpha(\lambda, n_a)} \frac{\delta(\lambda, n_a)}{\delta n_a} \qquad (11)$$

Here, $\alpha(\lambda, n_a)$ shows propagation loss, $\delta(\lambda, n_a)$ the loss difference, and n_a dielectric RI.

To investigate the wavelength sensitivity employing wavelength interrogation method to improve the sensor performance, Eq. (12) can be employed [27]:

$$S_\lambda = \frac{\Delta \lambda_{\text{peak}}}{\Delta n_a} \qquad (12)$$

Here, $\Delta \lambda$ and Δn_a represent the wavelength change of the peak resonance. The sensor resolution is an important parameter for detecting the small changes in analyte RIs.

It shows the identification capability of the offered sensor. The realization of the resolution of the sensor is expressed using Eq. (13) [28]:

$$R_S = \Delta n_a \times \frac{\Delta \lambda_{\min}}{\Delta \lambda_{\text{peak}}} (\text{RIU}) \tag{13}$$

Here, $\Delta \lambda_{\min}$ and $\Delta \lambda_{\text{peak}}$ represent the small spectral resolution and resonant peak shift. Sensor resolution is evaluated with negligible instrumental noise and extra noise generated by external disturbances. Figure of Merit (FoM) is also a crucial parameter. It can be expressed to evaluate the detection limit of the sensor with the help of Eq. (14) [29]:

$$\text{FoM} = \frac{\text{Sensitivity}}{\text{FWHM}} (\text{RIU}^{-1}) \tag{14}$$

Here, FWHM expresses full width at half maximum. For better detection limit, FoM should be high. It can be noticed that if the sensitivity rises and FWHM lowers, high FoM is achieved from the equation.

Optimization of Sensor

To measure the performance of the sensor, y-polarized fundamental core mode is preferred due to sharp and high loss peak in this propagation direction. The interpretation of the offered sensor can be calculated with optimized different geometrical parameters inclusive of silver (t_{Ag}) and TiO$_2$ layer thickness, pitch (p) size, and air hole diameters d_1, d_2, and d, respectively. To evaluate the impact of the performance change, a specific parameter has been changed while placing the other parameters constant.

Effect of Phase Matching and Distribution of EM Field

Photonic crystal fiber-based surface plasmon resonance works on the principle of guided evanescent field. Appropriately designed geometry of the core and cladding enhances the evanescent field propagation toward the metal surface. The free electrons get excited by the propagated wave that is incident on metallic film. When the wavelength or frequency of the guided core field is equal to the wavelength or frequency of the surface electrons, it generates SPW. The generated SPWs have been notably sensitive to the near RI. So, to identify the variation in RW, amplitude, local RIs, and spectral mode are monitored appropriately. For a specific analyte with a rise of the wavelength, the effective RI of the core mode decreases significantly. In Fig. 2, the characteristics of phase matching of core and SPP mode have been depicted for RI of $n_a = 1.40$. Hence, it is noticed that the effective RI of the core (real portion) and SPP mode index is

equal and cut at wavelength 0.85 μm. So, 0.85 μm expresses a phase-matching wavelength, and resonance occurs at this position. Maximum power shifts from core mode to SPP mode at the resonance point can be seen as a sharp loss peak. With the rise of analyte RI, the resonance point has shifted red.

Effect of Silver and TiO$_2$ Thickness Variation

The thickness of the silver layer has a crucial role in the loss and sensitivity as the thickness of the metal layer has a remarkable effect on the RW change. Sensitivity and CL peak depend on metal film thickness. Hence, the effect of change of Ag thickness on the complete sensing performance has been evaluated. With variation in Ag thickness for different analyte refractive index $n_a = 1.39$, 1.40, 1.41, confinement loss peak has been investigated, respectively. From Fig. 3a, CL peak expresses a red shift with a rise of t_{Ag} varying from 45 to 55 nm. The maximum peak has been observed for thin layer of silver which results in strong coupling. From Fig. 3b it has been observed that for the value of $t_{\text{Ag}} = 55$ nm, the AS peak is maximum with the fixed thickness of TiO$_2$ layer $t_t = 5$ nm. So, the optimized thickness of the silver film is 50 nm. The effect of variation in the TiO$_2$ (t_t) film thickness on CL spectra for $n_a = 1.39$, 1.40, 1.41 is displayed in Fig. 3c. From Fig. 3d, the maximum AS peak is observed on the $t_t = 5$ nm film thickness. So, 5 nm is the optimized thickness of the t_t.

Effect of Pitch Variation

The impact of different pitch size on the loss peak and amplitude sensitivity is shown in Fig. 4. Hence, the loss spectrum reduces with an increase in pitch size because it raises the RI difference between core and cladding. Furthermore, increasing size of pitch results in a blue shift and reduces CL depth. CL spectra has been plotted and observed for different pitch changing from 2.9, 3, 3.1 μm for $n_a = 1.39$, 1.40, 1.41, respectively. The maximum CL spectra have been obtained for the pitch value of 2.9 μm as shown in Fig. 4a. At the value of pitch (p) = 3.1 μm, the maximum AS peak has been observed as shown in Fig. 4b. On the contrary, the sensing region has been restricted from 1.33 to 1.41. So, the pitch (p) = 3.0 μm is optimized pitch of the sensor.

Effect of Air Hole Diameter Variation

The maximum AS has been attained for $d_c = 0.145p$ because of strong coupling of core and SPP mode. So, d_c is optimized center diameter. The effect of regular air hole diameter d on CL spectra is expressed in Fig. 5a. It is clear that with increase of d from 0.5p, 0.6p, and 0.7p, the CL spectra has been increased for 0.6p and reduced for 0.7p, although
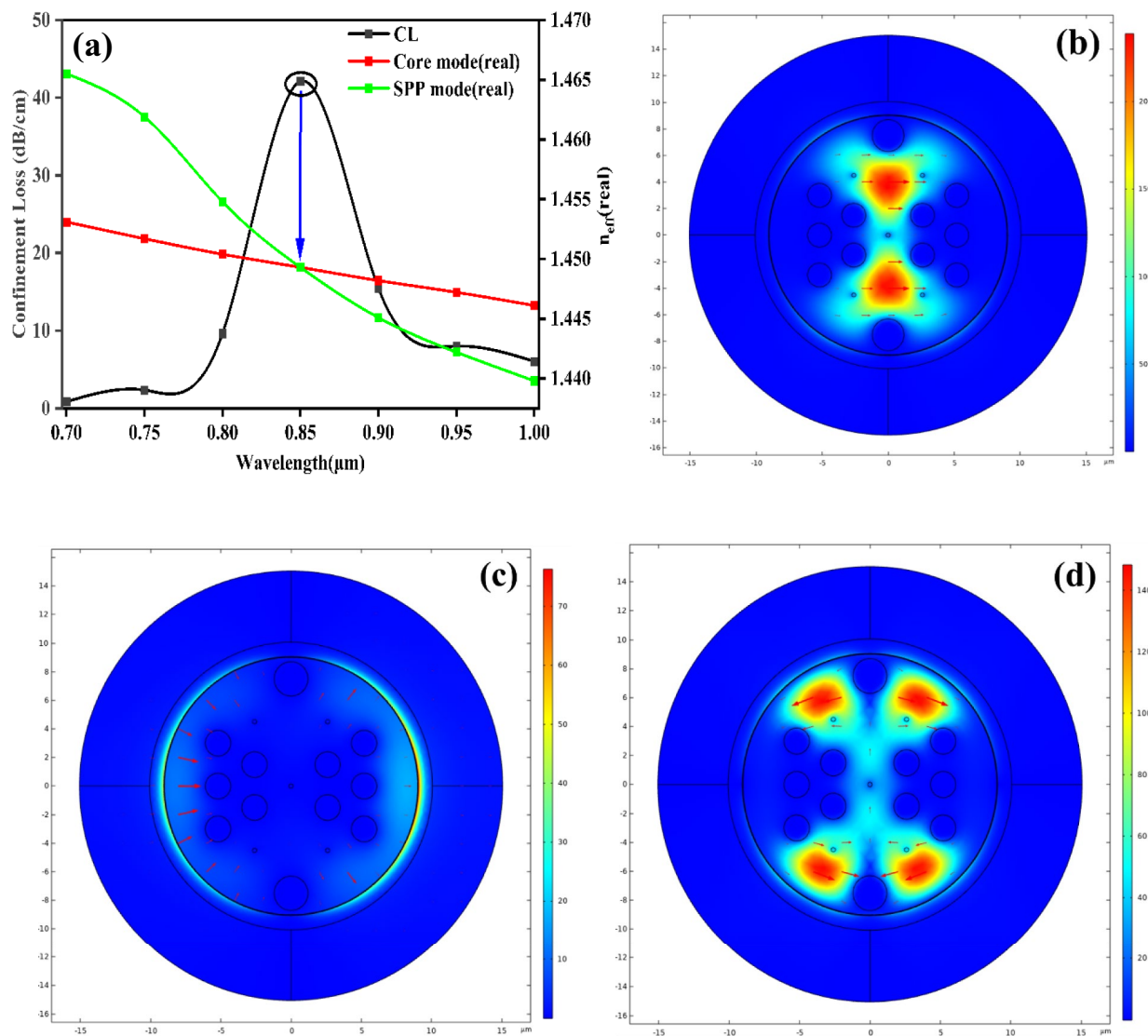
Fig. 2 **a** The phase matching effects and **b–d** EM field distributions for $n_a = 1.40$

no change has taken place in RW. From Fig. 5b, the highest AS peak has been observed for $n_a = 1.39$, 1.40, and 1.41, respectively. The impact of variation in the air hole diameter d_1 is shown in Fig. 5c. It has been noticed that the CL spectra has been decreased, when diameter d_1 has been scaled up from 0.7p to 0.8p which results in a redshift and conversely results in scaling up of d_1 from 0.8p to 0.9p. To maintain the proper spaces between the external ring and the metal surface, optimized air hole diameters are $d = 0.6p$ and $d_1 = 0.8p$. From Fig. 5d, it has been observed that the highest AS peak occurs with 0.7p, 0.8p, and 0.9p for $n_a = 1.39$, 1.40, and 1.41, respectively. Apart from this, the effect of air hole diameter d_2 contrast in the CL spectrum has been shown in Fig. 5e. It has been noticed that unchanged scaled-down air holes show inconsistency in the CL spectrum. Increasing the value of $d_2 = 0.05p$, 0.1p, and

0.15p shows a blue shift. Figure 5f shows that for $d_2 = 0.1p$, maximum AS has been achieved. So, $d_2 = 0.1p$ is the optimized diameter.

Sensing Performance with Variation of Different Analyte RIs

The CL and AS of the offered sensor employing optimized model parameters have been illustrated for various n_a with Eqs. (4) and (6) as shown in Fig. 6. The significant increase of n_a results in a small change of RI difference between core guided and plasmonic mode. Therefore, most evanescent waves travel through the cladding area rather than the core portion. Consequently, light the coupling improves through the metal surface and effectively interacts with the dielectric medium. So, the CL spectrum increases slowly and shifts
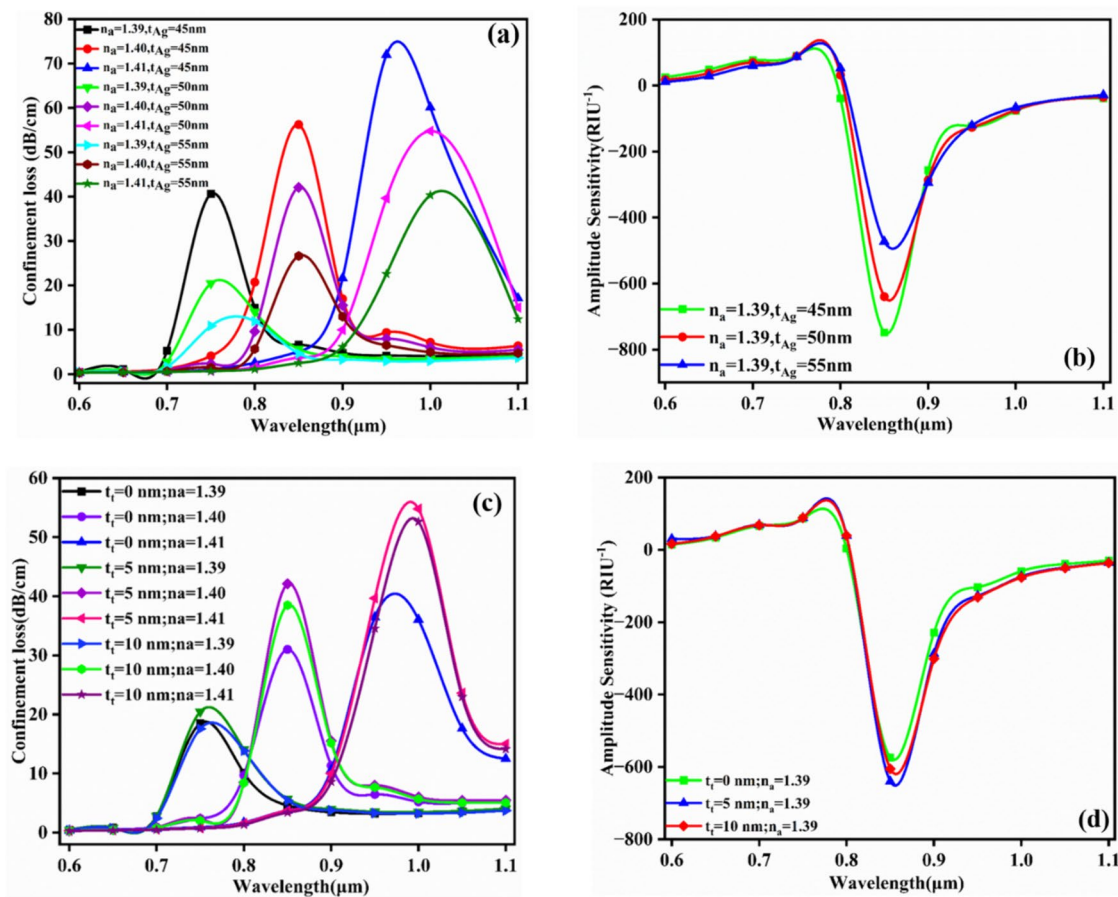
Fig. 3 **a**, **c** Confinement loss spectrum. **b**, **d** Amplitude sensitivity with the change in thickness of silver (t_{Ag}) and TiO$_2$ (t_t) layers

toward red. As the changing of analyte refractive index from $n_a = 1.36$ to 1.41, CL spectrum shifts toward maximum wavelength and significantly increases the RW peak as shown in Fig. 6.

Performance Analysis of the Sensor

After optimization of the sensor performance with the analyte medium refractive index, the proposed sensor has been
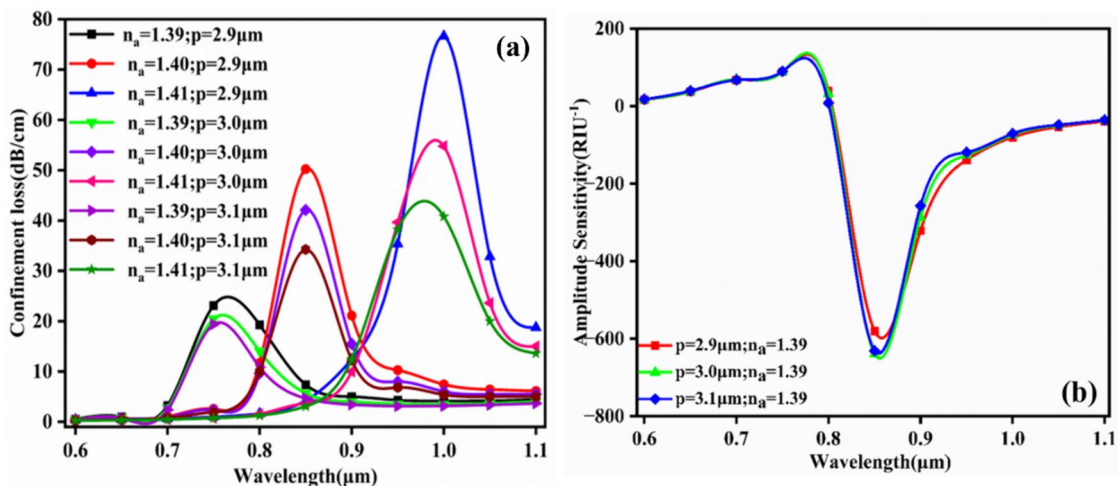

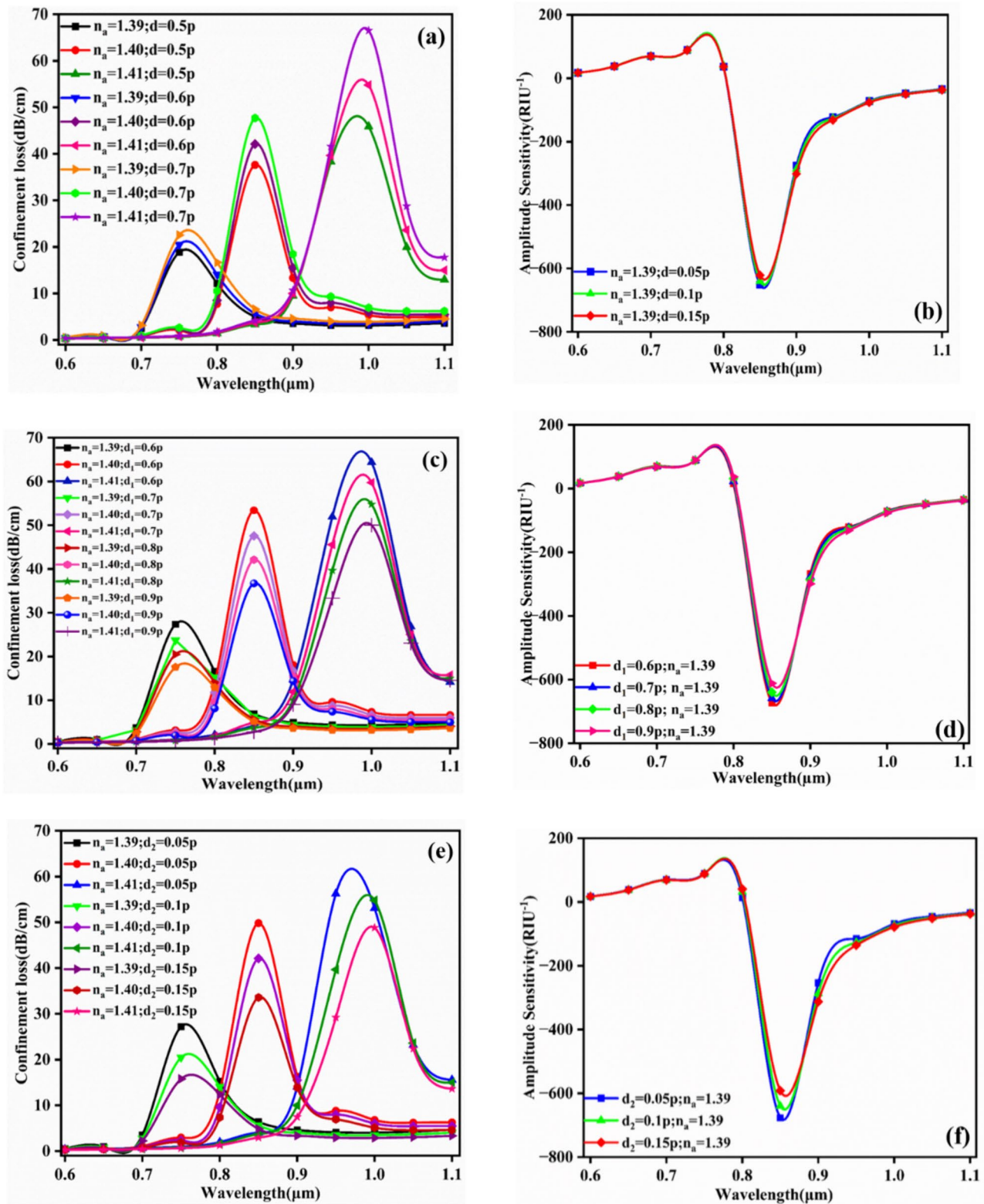**Fig. 4** **a** CL spectra. **b** Amplitude sensitivity with variation of pitch (p) size

Fig. 5 **a**, **c**, and **e** CL spectra. **b**, **d**, and **f** The spectrum of AS with variation of *d*, d_1, and d_2
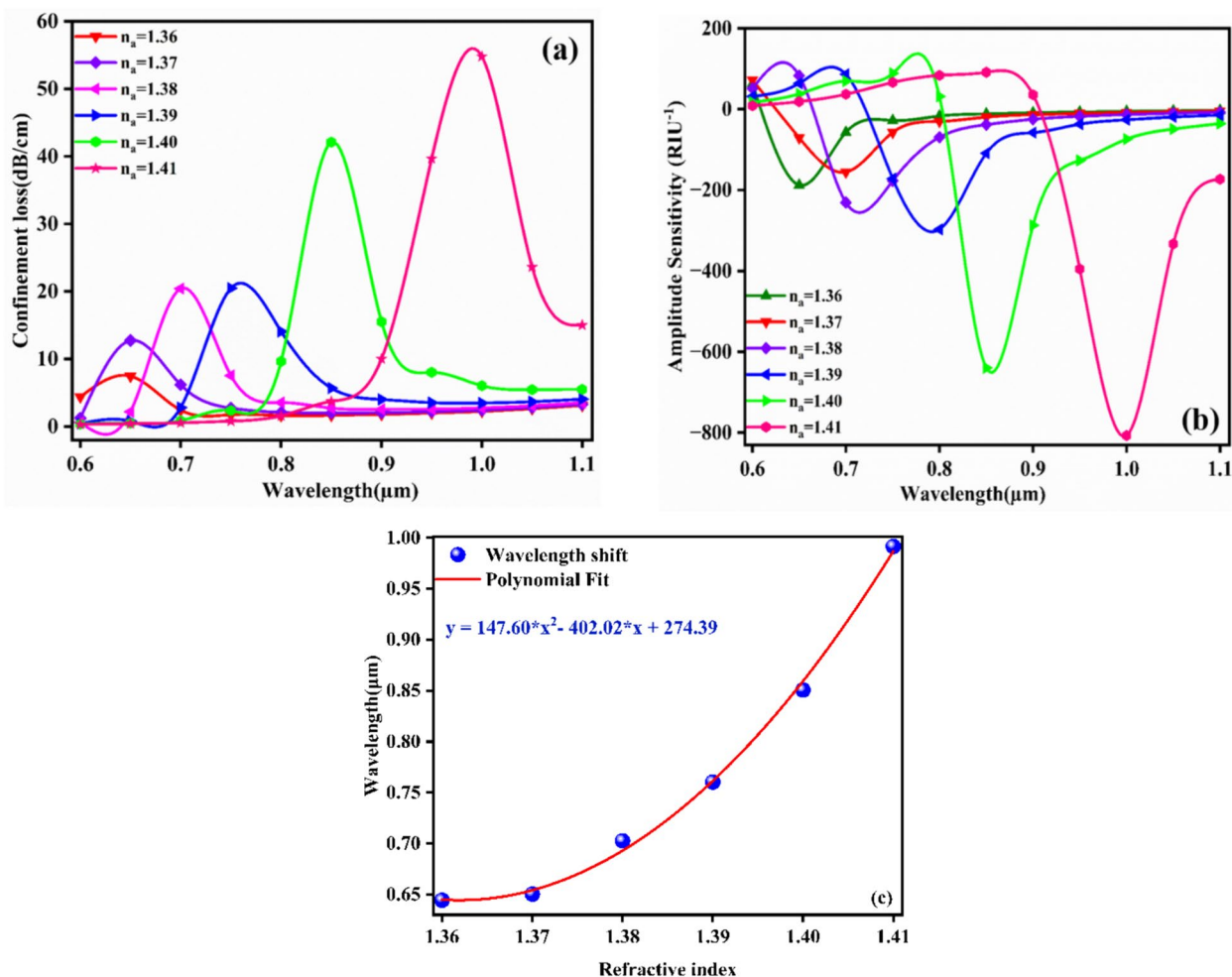
Fig. 6 Performance characteristics of the sensor. **a** CL spectra w.r.t the wavelength. **b** Amplitude sensitivity w.r.t the wavelength. **c** Wavelength sensitivity w.r.t the variation of n_a

employed to identify the bio-samples. For this purpose, different concentrations of the β-LG have been considered for the further analysis. The CL and AS can be noticed for the proposed sensor with variation of concentration of β-LG in Fig. 7. The spectral transition in resonance wavelength with variation in β-LG concentration (%) has been illustrated. In this instance, protein molecules have been filled throughout the height of the core area. In this situation, the spectral shift experiences a nearly exponential growth as the concentration of protein molecules rises.

Fabrication Feasibility and Applicability

The manufacturing process for the PCF sensor is notably intricate in comparison to traditional optical fibers. Various well-established fabrication methods, such as sol–gel, injection modelling, chemical vapor deposition (CVD), capillary stacking, atomic layer deposition (ALD), stack-and-drilling,

stack-and-draw, 3D printing, wheel polishing method (WPM), and extrusion techniques, are widely recognized [30]. A computer-controlled mill employing the drilling technique has been utilized to create air holes in the solid rod and solid tube, drawing them to form inside and outside air holes fibers, respectively [31]. Silver has been coated on the external layer of the microfiber employing the chemical vapor deposition (CVD) technique, while TiO2 has been coated on the inner layer of the fiber. To identify the unspecified sample with the effect of the metal surface a thickness of (0.5p) sensing layer has been positioned on the outer part of the silver layer. A thickness of 0.5p (10% of PCF's diameter) of a circular PML layer prevents the unapproved reflection of the light and absorbs the approaching evanescent wave from the PCF scattering boundary condition (SBC) which has been carried out.

For instance, an experiment briefly describes an Ag–TiO2-coated nanostructure in [32], changing the size and parameters of the layer. Furthermore, in the realm of

Fig. 7 **a** CL spectra. **b** Amplitude sensitivity. **c** Spectral shift in the resonance wavelength for distinct concentration with changing adlayer thickness in the core
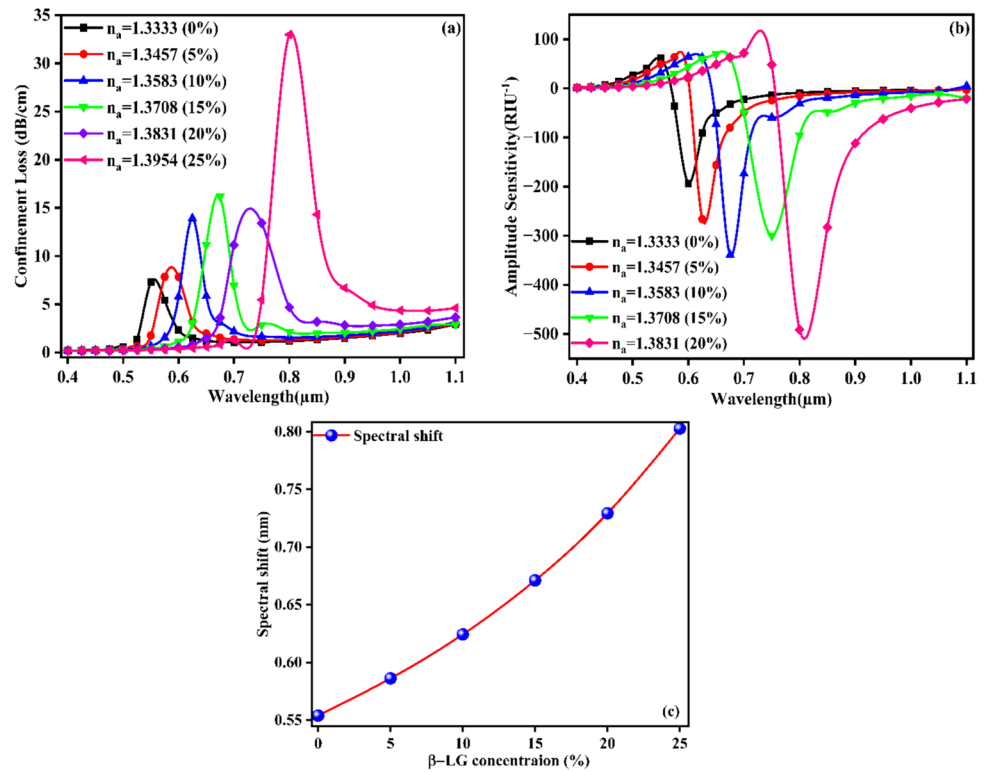
fabrication, several surface plasmon resonance-based optical fiber sensors with Au-deposited [33] and MgF$_2$/TiO$_2$-coated optical filters have been experimentally demonstrated [34].

In summary, the proposed sensor's extended operating wavelength period enhances its appeal for both telecommunications and sensing applications due to its short loss profile, concise, fabrication facility, and minimal back-reflection. For the application purpose, PCF-based SPR sensors find utility in bioimaging, organic chemical sensing, gas sensing, liquid sensing, tuberculosis detection, disease detection, glucose monitoring in urine, pregnancy testing, medical diagnostics, and environmental monitoring [35]. The suggested sensor, with an operating analyte ranging from 1.36 to 1.41, is well-suited for application as a

biosensor. Many biological analyte's refractive indexes fall within this range, including tuberculosis cell sensing ranging from 1.345 to 1.349 [36], pregnancy testing ranging from 1.335 to 1.343 [37], cancer cell detection ranging from 1.36 to 1.38 [38], alcohol sensing ranging from 1.333 to 1.3611 [39], and various blood component sensing (1.33–1.40) [24]. Consequently, the broad span of analytes and high sensing performance position the suggested sensor as a promising profile across numerous SPR-based biosensor application areas. For different range of RI and concentration of the analyte, the performance parameters are investigated in Tables 1 and 2, respectively. The performance parameter comparison in Table 3 has been incorporated with the recently reported articles.

Table 1 Performance parameters of the proposed sensor for various analyte RI

n_a	CL (dB-cm^{-1})	λ(μm)	$\Delta\lambda$(nm)	WS (nm-RIU^{-1})	AS$_{max}$ (RIU^{-1})	FWHM (nm)	FOM (RIU^{-1})	R_s (RIU)
1.36	7.71929	0.64443	05.91	591	67.95469	108.65488	05.43924	0.09154
1.37	12.96491	0.65034	52.33	5233	58.32204	75.46785	69.34078	0.80465
1.38	20.52631	0.70266	57.63	5763	3.41883	93.77383	61.45637	0.82168
1.39	21.22807	0.76029	90.23	9023	98.67764	71.33425	126.48903	1.18751
1.40	42.17543	0.85052	140.90	14,090	32.27955	82.90835	169.94669	1.65731
1.41	55.78947	0.99142	NA	NA	NA	84.91609	NA	NA

Table 2 Performance parameters of the proposed sensor for various concentration of β-LG

Concentration (%)	n_a	CL (dB-cm^{-1})	$\lambda(\mu m)$	$\Delta\lambda(nm)$	WS (nm-RIU^{-1})	AS$_{max}$ (RIU^{-1})	FWHM (nm)	FOM (RIU^{-1})
0	1.3333	7.63667	0.55392	32.32	2687.09677	12.72975	54.36753	0.46446
5	1.3457	8.84211	0.58624	38.12	3025.39683	47.24613	55.75544	0.71071
10	1.3583	14.10583	0.62436	46.75	3740	12.41961	42.93046	60.96525
15	1.3708	16.29569	0.67111	58.17	4729.26829	6.61539	55.36206	30.59572
20	1.3831	14.96972	0.72928	73.44	5970.73171	99.14327	95.30894	43.14451
25	1.3954	33.22198	0.80272	NA	NA	NA	78.23621	NA

Table 3 Performance comparison of the proposed sensor with existing sensors

Model	RI range	WS (nm-RIU^{-1})	AS$_{max}$ (RIU^{-1})	FWHM (nm)	FOM (RIU^{-1})	R_s (RIU)	Ref
Hexagonal PCF	1.33–1.36	4202.6	-	-	-	2.4×10^{-5}	[40]
Hollow core PCF	1.31–1.36	6000	-	-	857.1	2.5×10^{-5}	[41]
Dual side polished PCF	1.36–1.39	7142.86	-	-	-	3.33×10^{-5}	[42]
Double D-shaped dual-core PCF	1.26–1.42	7500	-	11.83	634.1	-	[43]
Dual-side polished PCF	1.30–1.40	9400	27.27	-	-	1.063×10^{-5}	[44]
Peripheral solid core	1.30–1.35	10,683.3	-	-	-	5.5×10^{-6}	[45]
Dual-core PCF	1.36–1.41	14,090	32.27955	82.90835	169.94669	1.65731	Proposed

Conclusion

The present paper offers a dual-core PCF-based SPR biosensor to identify the different concentration of in β-LG in the solution FEM-based numerical simulation methods which are a valuable tool for designing and predicting the optical behavior of biosensors. These approaches enable a swift prime evaluation of sensor performance and offer insights into the optical phenomena included and also lower the optimization and development expenses. In this regard of transmitting waves through intricate structures, the finite element method is the preferred choice. The comparison in Table 3 shows highest wavelength sensitivity of the proposed sensor with existing sensors. The proposed sensor gives maximum 98.67764 RIU^{-1}AS and 14,090 nm/RIU WS in the analyte sensing RI spectra from 1.36 to 1.41. It offers high FOM of 169.94669 RIU^{-1}. It also offers maximum AS of 99.14327 RIU^{-1} and WS of 5970.73171 nm/RIU with changing the concentration of β-LG.

Author Contributions Sapana Yadav: original manuscript writing, methodology, and software analysis; Yadvendra Singh: reviewing and conceptualization; Pooja Lohia and D. K. Dwivedi: editing and supervision.

Declarations

References

1. Khalil AE, El-Saeed AH, Ibrahim MA et al (2018) Highly sensitive photonic crystal fiber biosensor based on titanium nitride. Opt Quantum Electron 50:1–12. https://doi.org/10.1007/s11082-018-1397-0

2. Gangwar RK, Pathak AK, Kumar S (2023) Recent progress in photonic crystal devices and their applications: a review. Photonics 10:1199. https://doi.org/10.3390/photonics10111199

3. Salim ET, Fakhri MA, Tariq SM et al (2023) The unclad single-mode fiber-optic sensor simulation for localized surface plasmon resonance sensing based on silver nanoparticles embedded coating. Plasmonics. https://doi.org/10.1007/s11468-023-01949-z

4. Luan N, Yao J (2017) A hollow-core photonic crystal fiber-based SPR sensor with large detection range. IEEE Photonics J 9:1–7. https://doi.org/10.1109/JPHOT.2017.2694479

5. Mahmud I, Shushama KN, Khaleque A et al (2019) Highly sensitive plasmonic biosensor on photonic crystal fiber. IEEE Int Conf Telecommun Photonics ICTP 90:315–321. https://doi.org/10.1109/ICTP48844.2019.9041694

6. Al MM, Hossain MA, Haque E et al (2020) Dual-core photonic crystal fiber-based plasmonic RI sensor in the visible to near-IR operating band. IEEE Sens J 20:7692–7700. https://doi.org/10.1109/JSEN.2020.2980327

7. Manickam P, Senthil R (2023) Numerical investigation on the D-SPR-PQF — high refractive index and temperature sensor for

transport fuel adulteration. Results Phys 52:106883. https://doi.org/10.1016/j.rinp.2023.106883

8. Yadav S, Lohia P, Dwivedi DK (2023) A novel approach for identification of cancer cells using a photonic crystal fiber-based sensor in the terahertz regime. Plasmonics. https://doi.org/10.1007/s11468-023-01887-w

9. Wu F, Thomas PA, Kravets VG et al (2019) Layered material platform for surface plasmon resonance biosensing. Sci Rep 9:1–10. https://doi.org/10.1038/s41598-019-56105-7

10. Rifat AA, Hasan MR, Ahmed R, Butt H (2017) Photonic crystal fiber-based plasmonic biosensor with external sensing approach. J Nanophotonics 12:012503. https://doi.org/10.1117/1.jnp.12.012503

11. Rifat AA, Ahmed R, Yetisen AK et al (2017) Photonic crystal fiber based plasmonic sensors. Sens Actuators B Chem 243:311–325. https://doi.org/10.1016/j.snb.2016.11.113

12. Mustapha AA, Hassan OS, Ataro TD et al (2023) A wide-range transmission line-based linear displacement sensor. IEEE Sens J 23:18609–18623. https://doi.org/10.1109/JSEN.2023.3290912

13. Fan Z, Li S, Liu Q et al (2015) High sensitivity of refractive index sensor based on analyte-filled photonic crystal fiber with surface plasmon resonance. IEEE Photonics J 7:1–9. https://doi.org/10.1109/JPHOT.2015.2432079

14. Wang S, Lu Y, Ma W et al (2022) D-shaped surface plasmon photonic crystal fiber temperature sensor. Plasmonics 17:1911–1919. https://doi.org/10.1007/s11468-022-01683-y

15. Fan X-H, Zhang J-C, Zhang M et al (2017) Mid-infrared surface plasmon resonance sensor based on photonic crystal fibers. Opt Express 25:14238

16. Yadav S, Lohia P, Dwivedi DK (2023) Quantitative analysis of highly efficient PCF-based sensor for early detection of breast cancer cells in THz regime. J Opt. https://doi.org/10.1007/s12596-023-01404-6

17. Podder E, Hossain MB, Ahmed K (2022) Photonic crystal fiber for milk sensing. Sens Bio-Sensing Res 38:100534. https://doi.org/10.1016/j.sbsr.2022.100534

18. Ashley J, D'Aurelio R, Piekarska M et al (2018) Development of a β-lactoglobulin sensor based on SPR for milk allergens detection. Biosensors 8:1–11. https://doi.org/10.3390/bios8020032

19. Sajan SC, Singh A, Sharma PK, Kumar S (2023) Silicon photonics biosensors for cancer cells detection - a review. IEEE Sens J 23:3366–3377. https://doi.org/10.1109/JSEN.2023.3235920

20. Kumari S, Tripathi SM (2022) Hybrid plasmonic SOI ring resonator for bulk and affinity bio - sensing applications. SILICON 14:11577–11586. https://doi.org/10.1007/s12633-022-01877-3

21. Yadav S, Lohia P, Dwivedi DK (2023) Eminently sensitive mono-rectangular photonic crystal fiber-based sensor for cancer cell detection in THz regime. J Opt. https://doi.org/10.1007/s12596-023-01191-0

22. Yadav S, Singh S, Lohia P et al (2022) Delineation of profoundly birefringent nonlinear photonic crystal fiber in terahertz frequency regime. J Opt Commun. https://doi.org/10.1515/joc-2022-0143

23. Boopathi CS, Kumar KV, Sheeba Rani S et al (2018) Design of human blood sensor using symmetric dual core photonic crystal fiber. Results Phys 11:964–965. https://doi.org/10.1016/j.rinp.2018.10.065

24. Bijalwan A, Singh BK, Rastogi V (2021) Analysis of one-dimensional photonic crystal based sensor for detection of blood plasma and cancer cells. Optik (Stuttg) 226:165994. https://doi.org/10.1016/j.ijleo.2020.165994

25. Singh Y, Raghuwanshi SK (2019) Sensitivity enhancement of the surface plasmon resonance gas sensor with black phosphorus. IEEE Sensors Lett 3:18–21. https://doi.org/10.1109/LSENS.2019.2954052

26. Shakya AK, Singh S (2023) Novel Merger of spectroscopy and refractive index sensing for modelling hyper sensitive hexa-slotted plasmonic sensor for transformer oil monitoring in near-infrared region. Opt Quantum Electron 55:1–25. https://doi.org/10.1007/s11082-023-05016-z

27. Singh Y, Paswan MK, Raghuwanshi SK (2021) Sensitivity enhancement of SPR sensor with the black phosphorus and graphene with Bi-layer of gold for chemical sensing. Plasmonics 16:1781–1790. https://doi.org/10.1007/s11468-020-01315-3

28. Chaudhary VS, Kumar D, Mishra R, Sharma S (2020) Hybrid dual core photonic crystal fiber as hydrostatic pressure sensor. Optik (Stuttg) 210:164497. https://doi.org/10.1016/j.ijleo.2020.164497

29. Shakya AK, Singh S (2021) Design of dual polarized tetra core PCF based plasmonic RI sensor for visible-IR spectrum. Opt Commun 478:126372. https://doi.org/10.1016/j.optcom.2020.126372

30. Umar A, Singh S, Yadav S et al (2023) Numerical study of surface plasmon resonance biosensor using aluminium oxide and bismuth telluride nanomaterials for skin cancer cell detection. J Nanoelectron Optoelectron 17:1655–1658. https://doi.org/10.1166/jno.2022.3358

31. Bartkowiak D, Merk V, Reiter-Scherer V et al (2016) Porous MgF2-over-gold nanoparticles (MON) as plasmonic substrate for analytical applications. RSC Adv 6:71557–71566. https://doi.org/10.1039/c6ra10501g

32. Noman AA, Haque E, Hossain MA, Hai NH, Namihira Y, Ahmed F (2020) Sensitivity enhancement of modified D-shaped microchannel PCF-based surface plasmon resonance sensor. Sensors 20:6049. https://doi.org/10.3390/s20216049

33. Bhattacharya R, Rajan MSM, Sharafali A et al (2022) Experimental and theoretical study of polarization in commercially available photonic crystal fibers. Opt Quantum Electron 54:1–12. https://doi.org/10.1007/s11082-022-04066-z

34. Wang T, Mao Y, Liu B et al (2022) Compact fiber optic sensor for temperature and transverse load measurement based on the parallel vernier effect. IEEE Photonics J 14:1–8. https://doi.org/10.1109/JPHOT.2022.3206313

35. Chatterjee S, Deb U, Datta S et al (2017) Common explosives (TNT, RDX, HMX) and their fate in the environment: emphasizing bioremediation. Chemosphere 184:438–451. https://doi.org/10.1016/j.chemosphere.2017.06.008

36. Mohammed NA, Khedr OE, El-Rabaie ESM, Khalaf AAM (2023) High-sensitivity early detection biomedical sensor for tuberculosis with low losses in the terahertz regime based on photonic crystal fiber technology. Photonic Sensors 13:1–16. https://doi.org/10.1007/s13320-023-0675-z

37. Fontham ETH, Wolf AMD, Church TR et al (2020) Cervical cancer screening for individuals at average risk: 2020 guideline update from the American Cancer Society. CA Cancer J Clin 70:321–346. https://doi.org/10.3322/caac.21628

38. Miller KD, Fidler-Benaoudia M, Keegan TH et al (2020) Cancer statistics for adolescents and young adults, 2020. CA Cancer J Clin 70:443–459. https://doi.org/10.3322/caac.21637

39. Paul BK, Ahmed K, Asaduzzaman S, Islam MS (2017) Folded cladding porous shaped photonic crystal fiber with high sensitivity in optical sensing applications: design and analysis. Sens Bio-Sensing Res 12:36–42. https://doi.org/10.1016/j.sbsr.2016.11.005

40. Abbas FF, Ahmed SS (2023) Photonic crystal fiber pollution sensor based on the surface plasmon resonance technology. Baghdad Sci J 20:616–621. https://doi.org/10.21123/bsj.2022.6730

41. Divya J, Selvendran S (2023) Surface plasmon resonance-based gold-coated hollow-core negative curvature optical fiber sensor. Biosensors. https://doi.org/10.3390/bios13020148

42. Ibrahimi KM, Kumar R, Pakhira W (2024) Early detection of cancer cells using high-sensitivity dual-side polished photonic crystal fiber biosensors based on surface plasmon resonance.

Opt Quantum Electron 56:1–18. https://doi.org/10.1007/s11082-024-06782-0

43. Pravesh R, Kumar D, Pandey BP et al (2024) Design and analysis of a double D-shaped dual core PCF sensor for detecting biomolecules in the human body. IEEE Sens J XX: https://doi.org/10.1109/JSEN.2024.3380095

44. Ullah S, Chen H, Gao Z et al (2024) Dual-side polished surface plasmon resonance–based photonic crystal fiber for refractive index sensing and polarization filtering. Plasmonics. https://doi.org/10.1007/s11468-023-02185-1

45. Das S, Singh VK (2022) Highly sensitive PCF based plasmonic biosensor for hemoglobin concentration detection. Photonics Nanostructures - Fundam Appl 51:101040. https://doi.org/10.1016/j.photonics.2022.101040